Science
AAAS

Sidewinding with minimal slip: Snake and robot ascent of sandy slopes

Hamidreza Marvi *et al.*

Science **346**, 224 (2014);
DOI: 10.1126/science.1255718

This copy is for your personal, non-commercial use only.

If you wish to distribute this article to others, you can order high-quality copies for your colleagues, clients, or customers by clicking here.

Permission to republish or repurpose articles or portions of articles can be obtained by following the guidelines here.

The following resources related to this article are available online at www.sciencemag.org (this information is current as of October 9, 2014):

Updated information and services, including high-resolution figures, can be found in the online version of this article at:
http://www.sciencemag.org/content/346/6206/224.full.html

Supporting Online Material can be found at:
http://www.sciencemag.org/content/suppl/2014/10/08/346.6206.224.DC1.html

A list of selected additional articles on the Science Web sites **related to this article** can be found at:
http://www.sciencemag.org/content/346/6206/224.full.html#related

This article **cites 30 articles**, 16 of which can be accessed free:
http://www.sciencemag.org/content/346/6206/224.full.html#ref-list-1

This article has been **cited by** 1 articles hosted by HighWire Press; see:
http://www.sciencemag.org/content/346/6206/224.full.html#related-urls

This article appears in the following **subject collections:**
Physics, Applied
http://www.sciencemag.org/cgi/collection/app_physics

Downloaded from www.sciencemag.org on October 9, 2014

Science (print ISSN 0036-8075; online ISSN 1095-9203) is published weekly, except the last week in December, by the American Association for the Advancement of Science, 1200 New York Avenue NW, Washington, DC 20005. Copyright 2014 by the American Association for the Advancement of Science; all rights reserved. The title *Science* is a registered trademark of AAAS.

On the basis of our previous computational and experimental studies (*12*, *15*), we believe that sceptrin (**1a**) and ageliferin (**3a**) are derived from two hymenidin (**4b**, X=H) molecules whereas massadine (**2a**) is assembled from one oroidin (**4a**, X=H) and one dispacamide A (**4d**, X=OH) molecule (Fig. 1). The homodimerization (path a and b) and heterodimerization (path c) of **4** are enantiomeric pathways. The pathway selectivity is determined by the stability of the radical intermediates. The redox-neutral, reversible SET-promoted heterodimerization of **4a** and **4d** would give "pre-massadines" (**6**) with a C9 aminal group that is present in all [3+2] pyrrole–imidazole dimers (fig. S2). Although enantiomeric biosynthesis that produces both enantiomers of a natural product has been reported (*39*), enantiodivergent biosynthesis that produces opposite enantiomers of natural products as congeners described herein is unknown. This discovery may serve as a new guiding principle for protein engineering and catalyst design.

REFERENCES AND NOTES

1. A. Al-Mourabit, M. A. Zancanella, S. Tilvi, D. Romo, *Nat. Prod. Rep.* **28**, 1229–1260 (2011).
2. P. S. Baran, A. L. Zografos, D. P. O'Malley, *J. Am. Chem. Soc.* **126**, 3726–3727 (2004).
3. P. S. Baran, D. P. O'Malley, A. L. Zografos, *Angew. Chem. Int. Ed.* **43**, 2674–2677 (2004).
4. P. S. Baran, K. Li, D. P. O'Malley, C. Mitsos, *Angew. Chem. Int. Ed.* **45**, 249–252 (2005).
5. D. P. O'Malley, K. Li, M. Maue, A. L. Zografos, P. S. Baran, *J. Am. Chem. Soc.* **129**, 4762–4775 (2007).
6. J. Yamaguchi *et al.*, *Angew. Chem. Int. Ed.* **47**, 3578–3580 (2008).
7. D. P. O'Malley, J. Yamaguchi, I. S. Young, I. B. Seiple, P. S. Baran, *Angew. Chem. Int. Ed.* **47**, 3581–3583 (2008).
8. S. Su, I. B. Seiple, I. S. Young, P. S. Baran, *J. Am. Chem. Soc.* **130**, 16490–16491 (2008).
9. I. B. Seiple *et al.*, *Angew. Chem. Int. Ed.* **49**, 1095–1098 (2010).
10. S. Su, R. A. Rodriguez, P. S. Baran, *J. Am. Chem. Soc.* **133**, 13922–13925 (2011).
11. I. B. Seiple *et al.*, *J. Am. Chem. Soc.* **133**, 14710–14726 (2011).
12. X. Tan, C. Chen, *Angew. Chem. Int. Ed.* **45**, 4345–4348 (2006).
13. Z. Ma, J. Lu, X. Wang, C. Chen, *Chem. Commun.* **47**, 427–429 (2011).
14. X. Wang, Z. Ma, J. Lu, X. Tan, C. Chen, *J. Am. Chem. Soc.* **133**, 15350–15353 (2011).
15. X. Wang *et al.*, *J. Am. Chem. Soc.* **134**, 18834–18842 (2012).
16. L. E. Overman, B. N. Rogers, J. E. Tellew, W. C. Trenkle, *J. Am. Chem. Soc.* **119**, 7159–7160 (1997).
17. J. T. Starr, G. Koch, E. M. Carreira, *J. Am. Chem. Soc.* **122**, 8793–8794 (2000).
18. A. S. Dilley, D. Romo, *Org. Lett.* **3**, 1535–1538 (2001).
19. C. J. Lovely, H. Du, Y. He, H. V. Rasika Dias, *Org. Lett.* **6**, 735–738 (2004).
20. V. B. Birman, X.-T. Jiang, *Org. Lett.* **6**, 2369–2371 (2004).
21. H. Ding, A. G. Roberts, P. G. Harran, *Chem. Sci.* **4**, 303–306 (2013).
22. R. P. Walker, D. J. Faulkner, D. van Engen, J. Clardy, *J. Am. Chem. Soc.* **103**, 6772–6773 (1981).
23. S. Nishimura *et al.*, *Org. Lett.* **5**, 2255–2257 (2003).
24. A. Grube, S. Immel, P. S. Baran, M. Köck, *Angew. Chem. Int. Ed.* **46**, 6721–6724; 8107 (2007).
25. J. Kobayashi *et al.*, *Tetrahedron* **46**, 5579–5586 (1990).
26. P. A. Keifer *et al.*, *J. Org. Chem.* **56**, 2965–2975 (1991).
27. E. P. Stout, Y.-G. Wang, D. Romo, T. F. Molinski, *Angew. Chem. Int. Ed.* **51**, 4877–4881 (2012).
28. R. B. Kinnel, H.-P. Gehrken, R. Swali, G. Skoropowski, P. J. Scheuer, *J. Org. Chem.* **63**, 3281–3286 (1998).
29. B. H. Northrop, D. P. O'Malley, A. L. Zografos, P. S. Baran, K. N. Houk, *Angew. Chem. Int. Ed.* **45**, 4126–4130 (2006).
30. M. Köck, A. Grube, I. B. Seiple, P. S. Baran, *Angew. Chem. Int. Ed.* **46**, 6586–6594 (2007).
31. N. L. Bauld, *Tetrahedron* **45**, 5307–5363 (1989).
32. T. P. Yoon, *ACS Catal.* **3**, 895–902 (2013).
33. Z. Lu, T. P. Yoon, *Angew. Chem. Int. Ed.* **51**, 10329–10332 (2012).
34. D. Valentine Jr., G. S. Hammond, *J. Am. Chem. Soc.* **94**, 3449–3454 (1972).
35. F.-C. Chen *et al.*, *J. Polym. Sci., B, Polym. Phys.* **41**, 2681–2690 (2003).
36. J. Muñoz, C. Moriou, J.-F. Gallard, P. D. Marie, A. Al-Mourabit, *Tetrahedron Lett.* **53**, 5828–5832, 6865 (2012).
37. A. H. Hoveyda, D. A. Evans, G. C. Fu, *Chem. Rev.* **93**, 1307–1370 (1993).
38. J. T. Gautschi, S. Whitman, T. R. Holman, P. Crews, *J. Nat. Prod.* **67**, 1256–1261 (2004).
39. J. M. Finefield, D. H. Sherman, M. Kreitman, R. M. Williams, *Angew. Chem. Int. Ed.* **51**, 4802–4836 (2012).

ACKNOWLEDGMENTS

We thank M. Köck (Alfred Wegener Institute) for providing the natural samples of sceptrin and massadine, and J. Muñoz (Alfred Wegener Institute) for providing a copy of the CD spectrum of natural sceptrin•TFA. We also thank V. Lynch (University of Texas at Austin), J. Clardy (Harvard University), and T. Molinski (University of California, San Diego) for helpful discussions. The CD experiments were performed by H. Shi [University of Texas (UT) Southwestern]. Financial support was provided by NIH (NIGMS R01-GM079554 and R01-GM073949), the Welch Foundation (I-1596), and UT Southwestern. Metrical parameters for the structures of natural sceptrin (**1a**) and **21** are available free of charge from the Cambridge Crystallographic Data Centre under reference numbers CCDC-995387 (**1a**), 1014159 (**21**), and 1016848 (**21**).

SUPPLEMENTARY MATERIALS

www.sciencemag.org/content/346/6206/219/suppl/DC1
Materials and Methods
Figs. S1 to S10
Tables S1 to S5
References (*40*–*52*)
NMR spectra

6 May 2014; accepted 11 September 2014
10.1126/science.1255677

ANIMAL MOTION

Sidewinding with minimal slip: Snake and robot ascent of sandy slopes

Hamidreza Marvi,[1,2] Chaohui Gong,[3] Nick Gravish,[2] Henry Astley,[2] Matthew Travers,[3] Ross L. Hatton,[4] Joseph R. Mendelson III,[5,6] Howie Choset,[3] David L. Hu,[1,2,5] Daniel I. Goldman[2]*

Limbless organisms such as snakes can navigate nearly all terrain. In particular, desert-dwelling sidewinder rattlesnakes (*Crotalus cerastes*) operate effectively on inclined granular media (such as sand dunes) that induce failure in field-tested limbless robots through slipping and pitching. Our laboratory experiments reveal that as granular incline angle increases, sidewinder rattlesnakes increase the length of their body in contact with the sand. Implementing this strategy in a physical robot model of the snake enables the device to ascend sandy slopes close to the angle of maximum slope stability. Plate drag experiments demonstrate that granular yield stresses decrease with increasing incline angle. Together, these three approaches demonstrate how sidewinding with contact-length control mitigates failure on granular media.

The majority of terrestrial mobile robots are restricted to laboratory environments, in part because such robots are designed to roll on hard flat surfaces. It is difficult to systematically improve such terrestrial robots because we lack understanding of the physics of interaction with complex natural substrates such as sand, dirt, and tree bark. We are thus limited in our ability to computationally explore designs for potential all-terrain vehicles; in contrast, many of the recent developments in aerial and aquatic vehicles have been enabled by sophisticated computational-dynamics tools that allow such systems to be designed in silico (*1*).

Compared with human-made devices, organisms such as snakes, lizards, and insects move effectively in nearly all natural environments. In recent years, scientists and engineers have sought to systematically discover biological principles of movement and implement these in robots (*2*). This "bioinspired robotics" approach (*3*) has proven fruitful to design laboratory robots with new capabilities (new gaits, morphologies, and control schemes), including rapid running (*2*, *4*), slithering (*5*), flying (*6*), and swimming in sand (*7*). Fewer studies have transferred biological principles into robust field-ready devices (*4*, *8*) capable of operating in, and interacting with, natural terrain.

Limbless locomotors such as snakes are excellent systems to study to advance real-world all-terrain mobility. Snakes are masters of most terrains: They can move rapidly on land (*9*, *10*) and through water (*11*), burrow and swim through sand and soil (*12*), slither through tiny spaces (*13*), climb complex surfaces (*14*), and even glide through the air (*15*). Relative to legged locomotion, limbless locomotion is less studied, and thus broad principles that govern multi-environment movement are lacking. Recently

[1]School of Mechanical Engineering, Georgia Institute of Technology, Atlanta, GA, USA. [2]School of Physics, Georgia Institute of Technology, Atlanta, GA, USA. [3]Robotics Institute, Carnegie Mellon University, Pittsburgh, PA, USA. [4]School of Mechanical, Industrial, and Manufacturing Engineering, Oregon State University, Corvallis, OR, USA. [5]School of Biology, Georgia Institute of Technology, Atlanta, GA, USA. [6]Department of Herpetology, Zoo Atlanta, Atlanta, GA, USA.
*Corresponding author. E-mail: daniel.goldman@physics.gatech.edu

developed limbless robotic platforms (*5*), based generally on the snake body plan, are appealing for multifunctional robotics study because they are also capable of a variety of modes of locomotion. These robots can traverse confined spaces, climb trees and pipes, and potentially dive through loose material. However, the gaits that carry these robots across firm ground can be stymied by loose granular materials, collections of particles that display solidlike features but flow beyond critical (yield) stresses.

A peculiar gait called sidewinding is observed in a variety of phylogenetically diverse species of snakes (*9*, *16*). Animals with excellent sidewinding ability—such as the North American desert-dwelling sidewinder rattlesnake (*Crotalus cerastes*) in Fig. 1, A and C—are often found in environments that are either composed of granular materials (such as sand dunes) or are smooth, such as hardpan desert. Sidewinding is the translation of a limbless system through lifting of body segments while others remain in static (in the world frame, locally rolling/peeling in the frame of the body) contact with the ground. Such interactions minimize shear forces at contact, and thus, sidewinding is thought to be an adaptation to yielding or slippery surfaces (*16*). Biological measurements (*17*, *18*) indicate that relative to lateral undulation, rectilinear locomotion, and concertina motion, sidewinding confers energetic advantages on hard surfaces, mainly through lack of slip at the points of contact. But although sidewinding motion of biological snakes has been extensively studied on hard ground, (*16*, *17*, *19*, *20*), only one study has reported kinematics on granular media (*9*).

An initial robotic version of the sidewinding gait has proven useful to enable snake robots to maneuver over flat and bumpy terrain (*21*). In a robotic sidewinding mode, the device maintains two to three static (locally rolling/peeling) contacts with the substrate at any moment (*22*). During this motion, individual segments of the robot are progressively laid into ground contact, peeled up into arch segments, and then transferred forward to become new ground contact segments (*16*, *22*). However, when in field tests a limbless robot [which we will refer to as the Carnegie Mellon University (CMU) robot (Fig. 1, B and D)] was confronted with even modest granular inclines (≈10°) far from the maximum angle of stability (≈30°), it failed to climb (either slipping or rolling downhill).

We posit that the study of success and failure modes in biological snakes can improve the mechanics and control of limbless robot performance, whereas study of success and failure modes of robots can give insight into important mechanisms that enable locomotion on loose material and perhaps explain why sidewinding has evolved in such organisms. This idea builds on recent work using biologically inspired robots as "physical models" of the organisms; such models have revealed principles that govern movement in biological systems, as well as new insights into low-dimensional dynamical systems [for example, (*8*) and references therein].

To discover principles of sidewinding in loose terrain, we challenged *C. cerastes* (n = 6 snakes, mass = 98 ± 18 g, body length, tip-to-tail, L = 48 ± 6 cm) (*23*) to climb loose granular inclines (table S2) (*28*) of varied incline angle, in a custom trackway housed at Zoo Atlanta (fig. S2A). The data comprised 54 trials: six snakes, three inclinations, three trials each. Before each experiment, air flow through a porous rigid floor fluidized the granular media and left the surface of the sand in a loosely packed state with a smooth surface (movie S4); details of this technique are described in (*24*). Three high-speed cameras tracked three-dimensional (3D) kinematics of 8 to 10 marked points on the body. For systematic testing, we chose three incline angles, θ = 0°, 10°, and 20°; the maximum angle of stability θ_0 of the loosely packed material, where local perturbations resulted in system-wide surface flows, was θ_0 = 27°.

As shown in Fig. 1, A and C, and fig. S1A and as previously noted (*9*, *16*), on level granular media the snake generated two contacts (as highlighted by dashed lines in Fig. 1A) with the substrate at each instant, similar to the movement on hard ground (*16*, *17*). As shown in Fig. 1E, the sidewinding pattern could be approximated by posteriorly propagating waves in both horizontal (*xy*) and vertical (*yz*) planes, with a phase offset

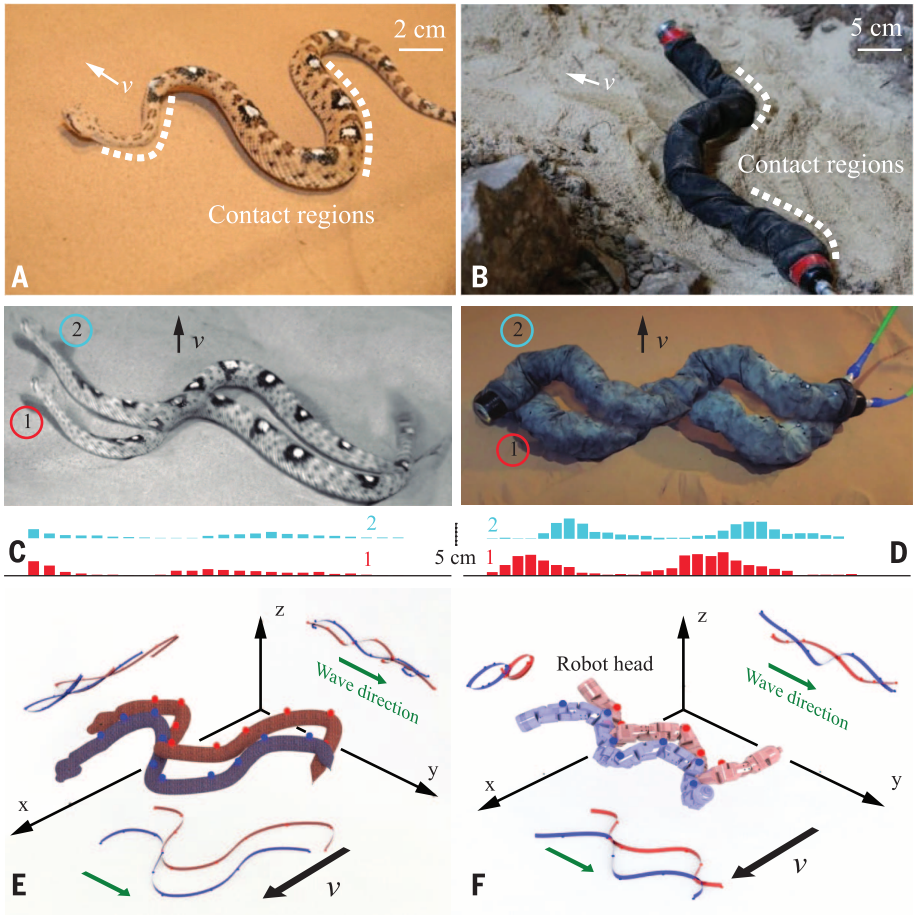

Fig. 1. Sidewinding locomotion on granular media. (**A**) A Sidewinder rattlesnake (*C. cerastes*) locomoting on a granular substrate of 20° inclination. (**B**) The CMU modular snake robot traversing granular media at ≈20° inclination. The arrow indicates the direction of motion. (**C** and **D**) Two superimposed snapshots of (C) a sidewinder and (D) the robot moving on level sand. The initial position is denoted by "1," and the successive position is denoted by "2." The time between snapshots in (C) and (D) is 0.2 and 3.1 s, respectively. The vertical bars beneath the images indicate vertical displacement along the body at the two times. (**E**) Two rendered snapshots of a snake sidewinding on level sand, with red indicating the initial time and blue a successive time; time between images is 0.2 s. The 3D configurations were reconstructed according to shape data collected from a sidewinder rattlesnake moving on level sand. Centerline projections of the 3D snake data are shown on three orthogonal planes. The *z* coordinates of the snake are scaled up four times to increase visibility in the *yz* and *xz* projections. The horizontal (*xy*) and vertical (*yz*) waves travel in the posterior direction of the snake with respect to a coordinate system rigidly attached to the animal (as shown by the green arrows). (**F**) Snapshots of the CMU snake robot executing a sidewinding gait on level sand and projections of the resultant body shapes onto three orthogonal planes. Red and blue indicate the initial and successive images, respectively. Time between images is 6.3 s. The horizontal and vertical waves travel in the posterior direction of the robot with respect to a body-fixed coordinate system (as shown by the green arrows).

of $\Delta\phi$ = 1.51 ± 0.17 rad. The position of contact points moved from head to tail, leaving pairs of straight parallel lines on the substrate. The angle between these lines and the direction of motion (fig. S4D) was α = 33 ± 8° on granular media. The length of each track line was the same as snake body length; the spacing of tracks was thus determined by the spacing of contact points on the snake's body (fig. S4C) (*16*). As previously observed on hard ground (*17*), speed increased with frequency (defined here as the number of cycles per second) (fig. 2C, inset). The snake body intruded into sand by 1.4 ± 1.3 cm and created a hill of material at each contact point; details on penetration depth measurement are provided in (*23*).

We next examined the behavior of the animals as θ increased. A sidewinder climbing an inclination of θ = 20° is shown in fig. S1A and movie S1. Unlike the robot, the snakes were able to ascend the granular inclines without any axial or lateral slip (movie S1), indicated by the horizontal regions in Fig. 2B. In addition, increasing θ did not significantly change the penetration depth [analysis of variance (ANOVA), $F_{2,51}$ = 0.33, P = 0.72], the angle between direction of motion and track lines (ANOVA, $F_{2,51}$ = 0.06, P = 0.81), or the number of contacts. Instead, we observed that as θ increased, the length of the contact regions relative to the body length increased (ANOVA, $F_{2,51}$ = 48.99, P < 0.0001); we refer to this quantity as l/L. To determine this quantity, we analyzed the 3D kinematics data to find the length of snake body in static (peeling) contact with sand in each cycle; details on contact length measurement are provided in (*23*). As shown in Fig. 2C, l/L increased by 41% as θ increased from 0° to 20°. At all θ, portions that were not in contact were lifted clear of the substrate. Wave frequency and climbing speed decreased with increasing θ (fig. S4, A and B) with effective step length S_t [defined as the distance the head moves forward in each period (fig. S4C)] remaining constant over all frequencies and θ. Further kinematic details of the movement are provided in the supplementary text.

To determine whether the ability to climb effectively on sandy inclines is common in closely related snakes, we examined the locomotor behavior of 13 species of pit vipers [subfamily Crotalinae (table S1)] in the collection of Zoo Atlanta on granular media. None of these species performed sidewinding in any conditions, instead using either lateral undulation or concertina, sometimes combined with rectilinear, gaits (table S1). On level sand, many species failed to achieve forward movement, and on sand slopes at θ = 10°, all but a single species failed to move uphill (Fig. 3C and movie S3). Yielding of the sand was accentuated by the failure of these species to lift portions of their body above the substrate (movie S3).

We hypothesize that the sidewinder rattlesnake's ability to move effectively on loose substrates (compared with the robot and the other closely related snakes) is made possible by neuromechanical control that generates appropriate contact length as sandy inclines become more susceptible to flow. To test this hypothesis, we next used the CMU robot as a physical model to study locomotor performance as a function of l/L for different θ (*23*). In particular, the CMU robot's ability to deform in arbitrary modes [using 17 modules (*23*), section 1.3], including a combination of traveling waves that generate sidewinding, makes it an attractive model on which to test the generality and efficacy of the contact length mechanism. And despite the differences in weight and size of the snake robot relative to the organism—as demonstrated in previous studies of fish, turtles, and cockroaches (*8*, *25*, *26*) (and shown below)—principles of small organism locomotor bio and neuromechanics can be deduced through systematic variation of parameters in larger-scale physical models.

To generate sidewinding in the robot, we controlled its modules (and joints) to generate two posteriorly directed traveling waves in the horizontal and vertical planes with a 1/4 period phase offset, $\Delta\phi$ = 1.57 rad (comparable with that of the animal). These waves were generated so that dorsal and ventral surfaces maintained their respective orientations throughout the motion. This produced a pattern of undulation and lifting similar to that observed in the biological snakes (Fig. 1, E and F). When the traveling waves are approximated by using sinusoids, the resultant shape of the robot resembles an elliptical helix whose minor axis is perpendicular to the ground and major axis is aligned with the direction of motion. Similar to the biological snake, during a gait cycle each module (segment) traced an approximately elliptical trajectory (Fig. 1F). All experiments were performed at constant wavelength (λ = 0.5L) and at frequencies sufficiently low as to avoid motor angular position and speed error.

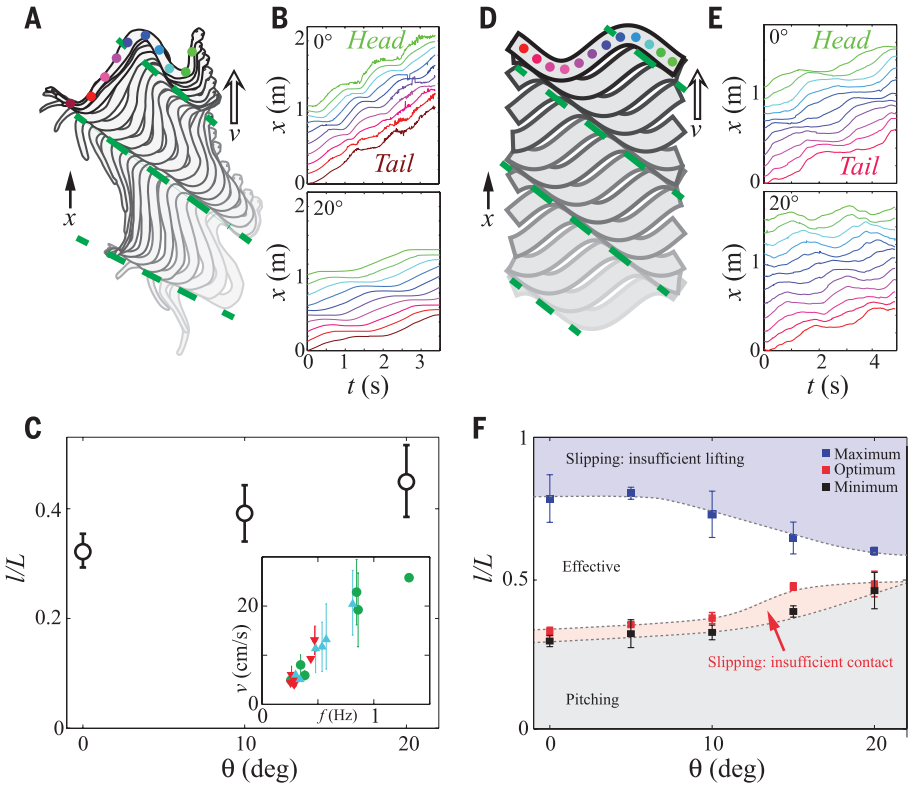

Fig. 2. Sidewinding motion at different granular incline angles θ. (**A**) Traces of the sidewinder rattlesnake (*C. cerastes*) sidewinding on level sand; green dashed lines indicate tracks that an animal leaves on sand. (**B**) Displacement versus time of the snake at θ = 0° (top) and 20° (bottom); colored lines correspond to colored dots on the snake in (A). Regions of each curve that have zero or near zero slope correspond to static contact with the granular medium. (**C**) Contact length l normalized by the body length L as a function of θ for sidewinder rattlesnakes. The data shown encompass six sidewinder rattlesnakes, with three trials per animal at each condition. (Inset) Snake forward speed v versus wave frequency f. Green circles, light blue triangles, and red upside down triangles correspond to θ = 0°, 10°, and 20°, respectively. Data are mean ± SD. (**D**) Illustration of the CMU snake robot sidewinding on level sand; green dashed lines indicate the tracks the robot leaves on the sand. (**E**) Displacement versus time of the robot at inclinations of 0° (top) and 20° (bottom); colored lines correspond to the colored dots on the robot in (D). The robot wave frequency in both of these plots was f = 0.31 Hz, and its normalized contact length was 0.53 ± 0.03 and 0.45 ± 0.05 for θ = 0° and 20°, respectively. (**F**) Minimum (black), optimum (red), and maximum (blue) normalized contact length l/L for successful robot climbs as a function of θ. The gray region below the minimum l/L corresponds to pitching failure. The pink region between the minimum and optimum l/L indicates slipping (but still maintains forward progress) due to insufficient contact, and the blue region above the maximum l/L indicates slipping failure due to insufficient lifting. Dashed lines are estimated boundaries of regions of different performance. The robot wave frequency for this plot was f = 0.08 Hz. l/L at several other wave frequencies are plotted in Fig. S6B. Data denote mean ± SD.

On level hard ground, a minor-to-major-axis aspect ratio of 0.9 produced steady motion at a speed of 0.03 m/s (at frequency f = 0.08 Hz). On hard surfaces at θ = 20°, decreasing the aspect ratio to 0.7 allowed the robot to climb without pitching or rolling down the hill and at comparable speeds as on level hard ground (*22*).

The waves that generated effective robot sidewinding on solid inclines were ineffective on granular media (movie S2). To improve the performance, we decreased the aspect ratio of the elliptical core, which increased the contact length in a manner analogous to the behavior observed in the biological snakes (fig. S6A). The minimum l/L needed for successful climbing (defined as ascending at positive forward speed without pitching; example traces are provided in Fig. 2D and tracked markers in Fig. 2E) increased by ≈70% as θ increased from 0° to 20°. Within the successful regions, we were further able to optimize the contact lengths to minimize slip and slightly improve the speed as compared with moving with the lower-bound of l/L. Details on robot contact length measurements are provided in (*23*). There was no dependence on frequency, indicating that body inertial forces were minimal and that granular frictional forces determined the resistive forces (*27*). Thus, despite the many differences between the biological and robot sidewinding, comparable performance was achieved through use of a similar strategy of increasing contact length with increases in θ. The elliptical helical gait is only one way to generate the traveling wave that propels the sidewinding in both hard ground and sand. Experimenting with helices of other cross-sections (such as oval shapes) led to similar results. Also, the maximum penetration depth d at the minimum l/L for successful climbing (at f = 0.08 Hz) decreased by ≈30% as θ increased from 0° to 20° (ANOVA, $F_{4,\,10} = 9.03$, $P = 0.007$).

We next systematically studied how robot performance changed with l/L (Fig. 3A). As shown in Figs. 2F and 3A, the robot was able to ascend effectively for a given θ only within a range of l/L. The range narrowed as θ increased, indicating that for shallow slope angles, sidewinding performance was robust to variations in contact length, whereas for higher slope angles, the control effort must increase to target a narrower range of contact length. On inclinations of <15°, the robot exhibited high performance (speed) in a wide range of l/L until too large l/L produced slipping that decreased forward speed; this was related to an inability of the robot to lift itself sufficiently to avoid unnecessary ground contact (similar to the slipping failures observed in other snake species). At the other extreme, small l/L resulted in an insufficient supporting region, causing the robot to pitch down the slope. In the pink region between minimum and optimum l/L in Fig. 2F, the robot slipped due to insufficient contact but still made forward progress. For large θ, even within the band of effective ascent, performance was degraded because of downhill slip, which decreased the effective step length (fig. S6D).

The success of the robot and its similar performance to the biological sidewinder suggest the following picture of sidewinding on sandy slopes. First, the animal targets a neuromechanical control scheme consisting of two independently controlled and appropriately phased orthogonal waves (Fig. 1, E and F). Such a scheme satisfies the definition of a "template"—that is, a behavior "contains the smallest number of variables and parameters that exhibits a behavior of interest" (*4*). Discovery of templates is useful because they provide an organizing principle for the enormous number of degrees of freedom inherent in all organisms. Second, the robot experiments suggest that the two-wave template dynamics can be simply modified on sandy slopes so that the animal targets a pattern of l/L and body-segment lifting that minimizes slip and pitching.

Understanding the ground reaction forces responsible for the relevant interactions (for example, optimal l/L without slip) requires a model of the interaction of objects with granular media. However, there is no fundamental theory for bio- and robotically relevant interactions in granular media and a wider class of materials (mud, rubble, or leaf litter). In particular, despite recent discoveries in terradynamics (*28*), drag (*27*), and impact (*29*) on level dry granular media [and

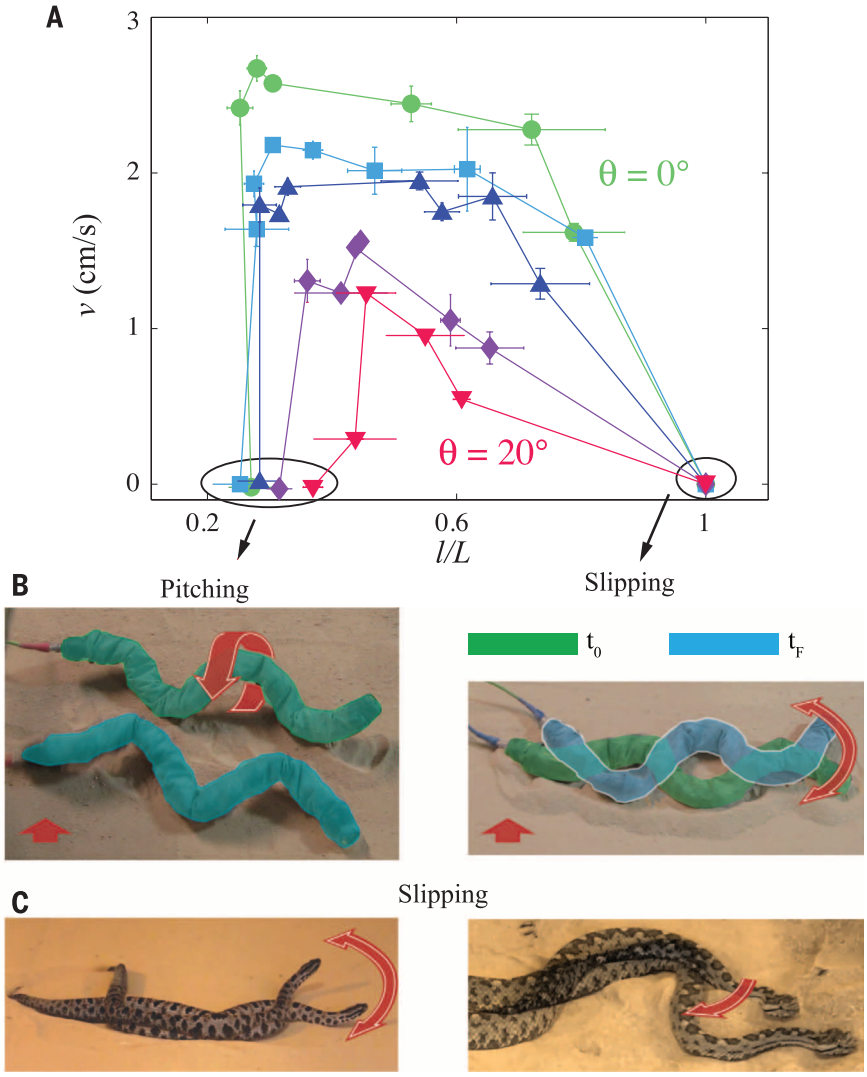

Fig. 3. Sensitivity of locomotor performance on granular media. (**A**) CMU snake robot speed versus l/L for inclination angles θ = 0° (green circles), 5° (light blue rectangles), 10° (dark blue triangles), 15° (purple diamonds), and 20° (red upside down triangles). Failure regimes due to pitching and slipping are circled in black. Three trials were performed at each condition. Data indicate mean ± SD. (**B**) Superimposed frames showing pitching and slipping failure modes in the robot ascending θ = 20° and 10° inclines, respectively. Uphill direction is vertically aligned with the page. t_0 and t_F represent the time at which each body configuration is captured. The time between two images in the pitching and slipping failure modes is 1.6 and 6.3 s, respectively. (**C**) Slipping failure of nonsidewinding snakes. Superimposed images show failed lateral undulation on level sand by *Sistrurus miliarius* (left, length 47 cm) and failed concertina locomotion on level sand by *Mixcoatlus melanurus* (right, length 47 cm). The time between two images of *S. miliarius* and *M. melanurus* is 0.5 and 9 s, respectively.

theoretical approaches to characterize granular rheology (*30*)], none of these studies have investigated drag forces on granular inclines.

We therefore studied the physics of transient granular yield forces as a function of θ. For context, studies of steady-state drag on level granular surfaces reveal that force is proportional to plate width, w, and depth squared, d^2 (*31*). To make the first measurements of drag force F dependence on θ, d, and w, we performed drag force measurements on granular inclines (*23*). We inserted flat plates of different widths (w = 1.5 to 6 cm) to different depths (d = 1 to 2 cm) into the granular medium perpendicular to the slope plane and displaced the plate downhill 15 cm. Depths were chosen to bound the range of penetration depths observed in the animal experiments. Because we were interested in the yield behavior of the granular slope in the quasi-static limit (we assume inertial effects are small at speeds at which the snakes generally operate), we performed drag at slow speeds and studied the force increases under small displacements δ from rest.

As shown in Fig. 4B, force increased substantially for small displacements until it reached a saturation regime, after which there was a slower increase in force associated with the buildup of a granular pile in front of the plate. We refer to the regime of rapid rise as the "stiffness" of the sand (before large yielding) and denote it k (F/δ near $\delta = 0$). We estimated k by fitting a line to the first 17% of data (corresponding to a displacement 0.5 cm, before material yielded noticeably) presented in Fig. 4B, and we plot this in Fig. 4C. For fixed d, k decreased by ≈50% as θ increased from 0° to 20° (Fig. 4C). For a fixed θ, k increased quadratically with d and nearly linearly with w. This scaling indicates that in the limit of shallow drag and small displacements δ, $F \propto k\,\delta$ with $k \propto w^{0.8}\, d^2 \cos\{[\pi/(2\theta_0)]\,\theta\}$, where the phenomenological cos term reflects the rapid decrease in force as θ approaches θ_0 [details on curve fitting are provided in (*23*)]. For θ = 0° and fixed δ, the dependence on w is similar to that previously observed (*31*), even though our depths are shallower.

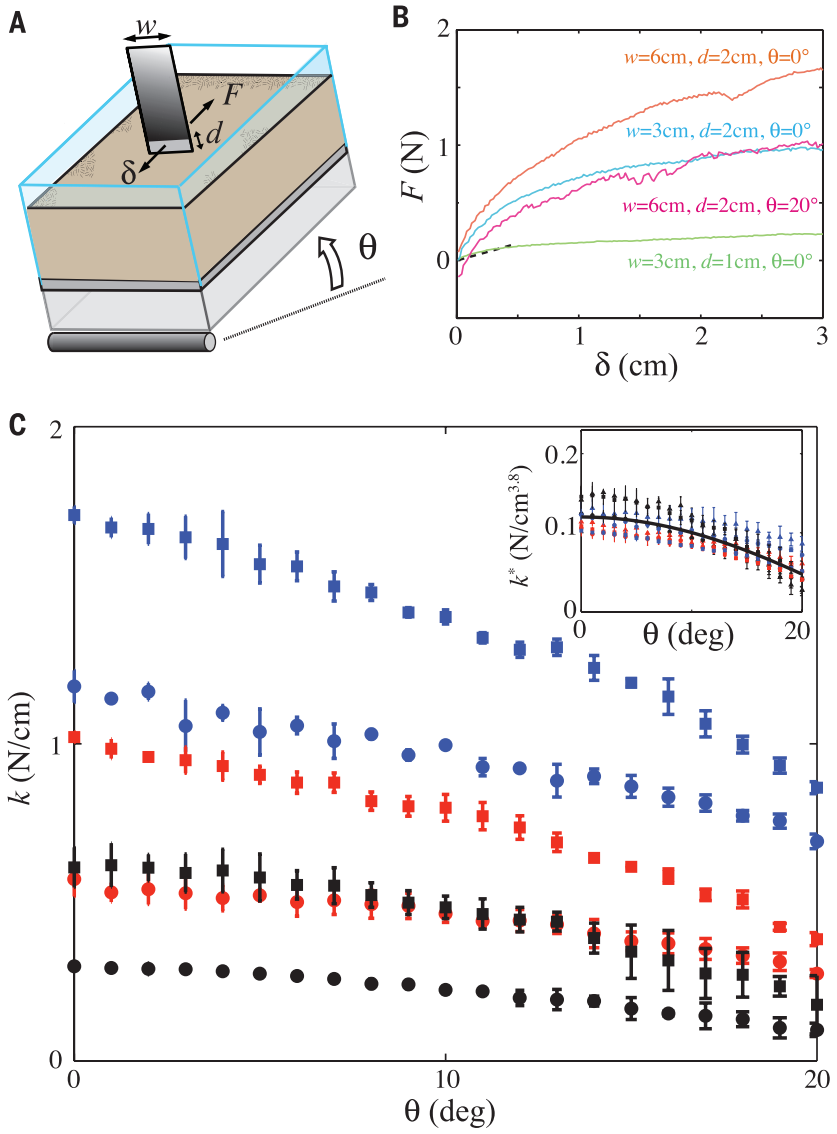

Fig. 4. Granular incline drag force experiments. (**A**) Schematic of drag force apparatus. (**B**) Drag force F versus horizontal displacement δ for different plate widths w and penetration depths d. The dashed line indicates the region used to calculate sand stiffness, k. (**C**) The fitted k versus inclination angle θ for different w and d. (Inset) The sand stiffness data collapse when normalized by $w^{0.8}d^2$; the thick black line is the fit function $0.12\cos([\pi/(2\theta_0)]\,\theta)$, with $\theta_0 = 0.47$ rad ($\theta_0 = 27°$). Triangles, circles, and squares represent w = 1.5, 3, and 6 cm, respectively. Black, red, and blue colors illustrate d = 1, 1.5, and 2 cm, respectively. Data denote mean ± SD.

The drag force measurements support our hypothesis of contact length control: As θ increases, effective sidewinding can be maintained by increasing the contact length to offset the decrease in yield forces. This allows the locomotor to maintain stresses below the yield stress, minimizing slip. Insights from the drag measurements also indicate why the appropriate amount of body lift and contact to be within the range of l/L is important. If lift is too small, other segments of the locomotor encounter drag forces that must then be offset by either increases in l/L, or potentially increasing intrusion depth. However, increases in l/L would decrease lift, resulting in greater drag. Increasing contact length relative to increasing intrusion depth has obvious benefits because intrusion into granular media requires yielding material, and the force to do so increases with depth [the challenges associated with penetration are described in (*32*)]. The energetic cost to vary l/L is small in comparison.

The contact length modulation strategy has benefits in terms of locomotor control: Once the animal or robot is moving using a sidewinding template (again, two independently controlled waves with phase difference of approximately π/2), slip and pitch mitigation in flowable substrates can be effected with relatively simple modulations of the basic template wave pattern. This control has features in common with our previous biological (*33*) and robotic (*24*, *26*) studies of relatively slow-legged movement on the surface of granular media, which also demonstrated that use of the solid features of granular media had benefits in certain locomotor regimes. We predict that other locomotors that move on granular surfaces could target movement patterns whose modulation can be used to achieve minimal-slip.

As expected, there were differences in the details between the sidewinding in the two systems. We view these differences, necessarily present because of the relative simplicity of the robot compared with the organism, as consequences of the different mechanisms that are used (biological complexity versus relative robot simplicity) as "anchors" of the templates, in the terminology discussed in (*8*). For example, the CMU robot has no compliance in its joints, many fewer degrees of freedom, and larger range of rotation (–90° to 90°) compared with those of biological snakes. Another interesting difference between a snake and the robot is that although both of them slowed as θ increased (figs. S4A and S6C), the snake's decrease in speed was correlated with

a decrease in frequency (indicating possibly either muscle limitations or active control to decrease inertial forces), whereas the robot speed decrease was largely determined by a decrease in spacing between tracks, as shown in fig. S6D. This decrease in effective step length was related to slipping of the robot at the highest θ. Comparative study of the anchoring mechanics is useful to learn about which lower-level mechanisms in the control hierarchy are critical, both to generate template dynamics as well as to understand neuromechanical control targets for the anchors.

REFERENCES AND NOTES

1. M. Costello, J. Sahu, *Proc. Inst. Mech. Eng. Part G J. Aerosp. Eng.* **222**, 1067–1079 (2008).
2. J. E. Clark *et al.*, *Proceedings of IEEE International Conference on Robotics and Automation* (2001), vol. 4, pp. 3643–3649.
3. B. Bhushan, *Philos. Trans. R. Soc. Math. Phys. Eng. Sci.* **367**, 1445–1486 (2009).
4. R. Playter, M. Buehler, M. Raibert, *Unmanned Ground Vehicle Technology VIII*, D. W. G. Grant R. Gerhart, Charles M. Shoemaker, Eds., vol. 6230 of *Proceedings of SPIE* (2006), pp. 6230201–6230206.
5. M. Tesch *et al.*, *Adv. Robot.* **23**, 1131–1158 (2009).
6. K. Y. Ma, P. Chirarattananon, S. B. Fuller, R. J. Wood, *Science* **340**, 603–607 (2013).
7. R. D. Maladen, Y. Ding, C. Li, D. I. Goldman, *Science* **325**, 314–318 (2009).
8. P. Holmes, R. J. Full, D. Koditschek, J. Guckenheimer, *SIAM Rev.* **48**, 207–304 (2006).
9. B. C. Jayne, *Copeia* **1986**, 915–927 (1986).
10. D. L. Hu, J. Nirody, T. Scott, M. J. Shelley, *Proc. Natl. Acad. Sci. U.S.A.* **106**, 10081–10085 (2009).
11. B. Jayne, *Copeia* **1985**, 195–208 (1985).
12. K. S. Norris, J. L. Kavanau, *Copeia* **1966**, 650–664 (1966).
13. H. Marvi, D. L. Hu, *J. R. Soc. Interface* **9**, 3067–3080 (2012).
14. G. Byrnes, B. C. Jayne, *J. Exp. Biol.* **213**, 4249–4256 (2010).
15. J. J. Socha, *Nature* **418**, 603–604 (2002).
16. W. Mosauer, *Am. Nat.* **64**, 179–183 (1930).
17. S. M. Secor, B. C. Jayne, A. F. Bennett, *J. Exp. Biol.* **163**, 1–14 (1992).
18. H. Marvi, J. Bridges, D. L. Hu, *J. R. Soc. Interface* **10**, 20130188 (2013).
19. J. Gray, *J. Exp. Biol.* **23**, 101–120 (1946).
20. B. C. Jayne, *J. Exp. Biol.* **140**, 1–33 (1988).
21. J. Burdick, J. Radford, G. Chirikjian, *Adv. Robot.* **9**, 195–216 (1994).
22. R. L. Hatton, H. Choset, *IEEE International Conference on Robotics and Automation* (2010), pp. 691–696.
23. Materials and methods are available as supplementary materials on *Science* Online.
24. C. Li, P. B. Umbanhowar, H. Komsuoglu, D. E. Koditschek, D. I. Goldman, *Proc. Natl. Acad. Sci. U.S.A.* **106**, 3029–3034 (2009).
25. S. Sefati *et al.*, *Proc. Natl. Acad. Sci. U.S.A.* **110**, 18798–18803 (2013).
26. N. Mazouchova, P. B. Umbanhowar, D. I. Goldman, *Bioinspir. Biomim.* **8**, 026007 (2013).
27. R. Albert, M. Pfeifer, A.-L. Barabási, P. Schiffer, *Phys. Rev. Lett.* **82**, 205–208 (1999).
28. C. Li, T. Zhang, D. I. Goldman, *Science* **339**, 1408–1412 (2013).
29. H. Katsuragi, D. J. Durian, *Nat. Phys.* **3**, 420–423 (2007).
30. D. L. Henann, K. Kamrin, *Proc. Natl. Acad. Sci. U.S.A.* **110**, 6730–6735 (2013).
31. D. J. Costantino, J. Bartell, K. Scheidler, P. Schiffer, *Phys. Rev. E Stat. Nonlin. Soft Matter Phys.* **83**, 011305 (2011).
32. A. G. Winter 5th, R. L. H. Deits, A. E. Hosoi, *J. Exp. Biol.* **215**, 2072–2080 (2012).
33. N. Mazouchova, N. Gravish, A. Savu, D. I. Goldman, *Biol. Lett.* **6**, 398–401 (2010).

ACKNOWLEDGMENTS

We thank M. Tesch, E. Cappo, J. Rembisz, and L. Li from Robotics Institute at Carnegie Mellon University for helping with the robot experiments; J. Brock, D. Brothers, R. Hill, L. Wyrwich, and B. Lock from Zoo Atlanta for helping with snake experiments; A. Young and K. Young for assistance with collecting snakes; D. Dimenichi, R. Chrystal, and J. Shieh from Georgia Institute of Technology for helping with construction and video analysis; T. Nowak and C. Hobbs for photography; V. Linevich for CAD drawings; P. Umbanhowar and A. Zangwill for helpful discussion; the National Science Foundation (NSF) (CMMI-1000389, PHY-0848894, PHY-1205878, and PHY-1150760); Army Research Office under grants W911NF-11-1-0514 and W911NF1310092; the Army Research Lab Micro Autonomous Systems and Technology Collaborative Technology Alliance under grant W911NF-08-2-0004; and the Elizabeth Smithgall Watts endowment, for financial support. D.I.G., H.C., and D.H. also acknowledge the Army Research Office and NSF Physics of Living Systems for supporting the Locomotion Systems Science Workshop in Arlington, Virginia, May 2012. The data collected for this study will be made available through the SMARTech data repository at Georgia Institute of Technology.

SUPPLEMENTARY MATERIALS

www.sciencemag.org/content/346/6206/224/suppl/DC1
Materials and Methods
Figs. S1 to S6
Tables S1 and S2
References (*34–38*)
Movies S1 to S5

7 May 2014; accepted 1 August 2014
10.1126/science.1255718

ECONOMIC DEMOGRAPHY

Is low fertility really a problem? Population aging, dependency, and consumption

Ronald Lee,[1]* Andrew Mason,[2,3]* members of the NTA Network†

Longer lives and fertility far below the replacement level of 2.1 births per woman are leading to rapid population aging in many countries. Many observers are concerned that aging will adversely affect public finances and standards of living. Analysis of newly available National Transfer Accounts data for 40 countries shows that fertility well above replacement would typically be most beneficial for government budgets. However, fertility near replacement would be most beneficial for standards of living when the analysis includes the effects of age structure on families as well as governments. And fertility below replacement would maximize per capita consumption when the cost of providing capital for a growing labor force is taken into account. Although low fertility will indeed challenge government programs and very low fertility undermines living standards, we find that moderately low fertility and population decline favor the broader material standard of living.

Economic behavior, abilities, and needs vary strongly over the human life cycle. During childhood and old age, we consume more than we produce through our labor. The gap is made up in part by relying on accumulated assets. It is also made up through intergenerational transfers, both public and private, that shift resources from some generations to others with no expectation of direct repayment. Private transfers occur when parents rear their children and when older people assist their adult children or receive assistance from them. Public transfers include public education, publicly funded health care, public pensions, and the taxes to pay for these programs. Because of these economic interdependencies across age, fertility rates that are falling or already low will drive rapid population aging in economies around the world. Forty-eight percent of the world's people live in countries where the total fertility rate (TFR) was below replacement, about 2.1 births per woman for 2005 to 2010. The TFR is 1.5 births per woman in Europe and 1.4 births per woman in Japan (*1*). With fertility this low, population growth will give way to population decline, and population aging will be rapid. The median age of the Southern European population, for example, is projected to reach 50 years of age by 2040 as compared to 41 in 2010 and 27 in 1950 (*1*). In 2013, governments in 102 countries reported that population aging was a "major concern," and 54 countries had enacted policies intended to raise fertility (*2*).

This is a remarkable reversal from decades of concern about the economic and environmental consequences of high fertility and rapid population growth (*3*). Should we now be alarmed about low fertility, population decline, and population aging? Should governments encourage their citizens to bear more children to balance the dramatic future increase in the number and proportion of elderly?

Identifying an optimal population policy is likely to be impossible for several reasons. First, children yield direct satisfaction and impose

[1]Department of Demography and Department of Economics, University of California, 2232 Piedmont Avenue, Berkeley, CA 94720, USA. [2]Department of Economics, University of Hawaii at Manoa, 2424 Maile Way, Honolulu, HI 96821, USA. [3]East-West Center, 1601 East-West Road, Honolulu, HI 96848-1601, USA.
***Corresponding author. E-mail: rlee@demog.berkeley.edu (R.L.); amason@hawaii.edu (A.M.)** †National Transfer Accounts (NTA) Network authors with their institutions appear at the end of this paper.

www.sciencemag.org/content/346/6206/224/suppl/DC1

Supplementary Material for

Sidewinding with minimal slip: Snake and robot ascent of sandy slopes

Hamidreza Marvi, Chaohui Gong, Nick Gravish, Henry Astley, Matthew Travers, Ross L. Hatton, Joseph R. Mendelson III, Howie Choset, David L. Hu, Daniel I. Goldman*

*Corresponding author. E-mail: daniel.goldman@physics.gatech.edu

Published 10 October 2014, *Science* **346**, 224 (2014)
DOI: 10.1126/science.1255718

This PDF file includes:

Materials and Methods

Figs. S1 to S6

Table S1

Full Reference List

Other Supplementary Material for this manuscript includes the following:
(available at www.sciencemag.org/content/346/6206/224/suppl/DC1)

Movies S1 to S4

Materials and Methods

Snakes, fluidized bed, visualization, and tracking

Data was collected for six adult sidewinder rattlesnakes, *Crotalus cerastes* (N = 6, m = 98±18 g, L = 48±6 cm) and 200 kg of sand from Yuma County, Arizona (Fig. S1a). All of these snakes were housed at Zoo Atlanta where the experiments were conducted. We designed and built an air-fluidized bed (Fig. S2a) of size 2 x 1 m^2 to control the sand compactness (volume fraction) and inclination angle. In the fluidized bed, above a critical air flow rate (against gravity), the granular material behaves like a fluid. Gradually decreasing the flow to zero results in the media reaching a loosely packed state with a flat surface; previous disturbances to the medium are no longer present. Air flow was turned off during experiments.

We recorded kinematic shape change data (snake and robots) using 3 AOS X-PRI high speed cameras at 120 fps. We calibrated the cameras, analyzed all of the videos, and obtained the position of each dot on snake body as a function of time using an automated image processing software developed in MATLAB (*34*). We used a calibration object with 49 markers (Fig. S2b) to calibrate our 3 cameras. As detailed in the Contact length measurement section, we used the 3D shape data to find the portion of the animal's body in contact with sand. Penetration depth was obtained based on the *z*-displacement of the dots on snake body; see penetration depth measurement section for details. Body speed was measured as distance traveled per unit of time averaged over all points tracked on the snake's body; regularization was performed such that contributing measurements were taken from periods where the average gait frequency varied by less than 10%. The wave frequency was found by analyzing the *x*-displacement data using a peak detection algorithm (*18*). To determine the phase offset between *xy* and *yz* waves we found the phase of horizontal wave (*xy*) at the static regions of body. We know the phase of vertical wave (*yz*) at the center of these static regions since they correspond to the lowest point of a wave. We assumed a sinusoidal curvature and determined *xy* phase of the static regions based on the body curvature and its rate of change at these points. The mean of these *xy* phase values was the center of the static region, corresponding to the lowest point in the vertical wave.

Contact length measurement

We provide a more detailed description of our methods for measuring contact length of the snake and snake robot. The MATLAB program DLTdv4 (*34*) was used to analyze synchronized videos, recorded using 3 AOS high-speed cameras, to obtain time resolved *xyz* positions of tracking dots on the dorsal surface of the snake's body (Fig. 2b,e). We tested the accuracy of this method by putting 5mm spherical markers at known *xyz* positions on sand and computing their positions in the tracking software. The *xyz* coordinates of these markers were determined to within 2mm (the penetration depth of snakes were on the order of 1.4 ± 1.3 cm). Although the snakes generate continuous traveling waves as they move, parts of the body form regions in static contact with the substrate (unless the material yields). These instantaneously static segments roll/peel away from the substrate as the snake moves. This process is similar to a slip-free wheel, which makes instantaneous static contact with the ground as it rolls. The fact that these

regions are in static contact is shown by observation of snake ventral scale imprints on the sand (see Fig. S2c).

Thus, to obtain the normalized contact length for the snakes, we must find the proportion of the snake body that has zero velocity at each instant. Using our digitally tracked 3D points we determined snake-ground contacts by examining the velocity profile along the body of the snake. We calculated the numerical time derivative of displacement in the direction of travel for each dot on the snake's body. We then found the proportion of time this derivative was below a manually tuned threshold in each period (Fig. 2b,e). We averaged this proportion for all of the dots on each snake in each trial. We report this average as the proportion of time the snake was in contact with the ground in each trial. According to the following discussions this parameter is equal to the portion of snake length that is in contact with sand, which we call the normalized contact length l/L.

We assume wave speed and contact length stay constant in a gait cycle, and any point on the substrate is touched only once by the snake body. As the wave travels down the snake body, the amount of time that a particular marker is static, t_s is proportional to the length of contact, $l/L = t_s/T$. As discussed above, we determined t_s/T (the length of horizontal segments of the plots in Fig. 2b divided by the period T) and averaged over all of the markers to calculate the normalized contact length l/L.

To find the contact segments for the snake robot we stopped the robot at the same phase after each trial and directly measured the robot-sand contact length. This contact length was independent of the phase at which we stopped the robot (all experiments were performed at constant wavelength ($\lambda = 0.5L$)). This direct measurement removed the need for 3D data analysis.

In addition, we used video inspection to validate our contact length calculations. We used open source Tracker, a video analysis and modeling tool (https://www.cabrillo.edu/~dbrown/tracker/), to manually analyze each video and estimate the portion of snake and robot body that was in contact with the sand in each trial. The manual video inspection proceeded in the following steps: We opened the video of interest in Tracker. We then chose a configuration/phase of the animal that is easy to visualize the segments that make contact with sand; see Fig. S1 (we consistently used the same configuration for all of the videos, although contact length remains constant during each period). We then manually measured the length of body in contact relative to the entire length of the animal. Regions of the snake body in which a visual shadow below the body were observed were classified as the lifted segments of the body, the portions of the snake body which were in contact with the sand did not have a shadow and were often signified by a lack of body curvature in these regions. The equally spaced dots we placed on the snake's body helped us estimate the normalized contact length. As shown in Fig. S1, the contact regions were clear from the side view and were consistent between different trials (small error bars in Fig. S3a). As shown in Fig. S3a,b the results of the manual video inspection were consistent with our previously reported data for contact length of snake/robot.

Penetration depth measurement

We found penetration depth of snakes using the z-displacement of the markers on the snake's body using the visual tracking system discussed above. We assumed a

constant dorsoventral thickness for the snakes and searched for the maximum *z*-displacement of the markers in each trial and defined this as penetration depth. However, we needed to know where the sand surface was relative to an inertial frame to get accurate *xyz* coordinates of the markers. Thus, before each trial we fluidized the bed to obtain a uniformly flat granular surface with minimal variation from trial to trial. Our experimental test bed was constructed specifically for this purpose, with a porous floor along the entire bottom area so uniform air flow through the sand is possible. This resulted in the creation of a uniform and repeatable granular surface for each trial. The air fluidization technique has been used in studies of locomotion on granular media to construct such environmental initial conditions (*7*, *24*).

Granular

Granular drag experiments were performed in an air fluidized bed of length, L = 43 cm, and width, W = 28 cm, filled with the same sand used in the snake and robot experiments. Air flow through a porous floor in the bed fluidized the sand into a loosely packed granular state consistent with that used in locomotion experiments. After fluidization and once the sand settled, we slowly (0.9 degrees/s) tilted the bed to an angle between 0 − 20 degrees. A flat plate of width, w = 1.5 − 6 cm, was inserted to a depth d = 1 − 2 cm and displaced a distance of 6 cm at a speed of 0.65 cm/s along the sand slope. Plate displacement was performed by a Firgelli L16 miniature linear actuator. The flat plate was constructed of 1 mm thick aluminum; four strain gauges (Omega KFG) were attached to the top of the plate. Using the strain measurements, we were able to extract the granular drag force experienced by the flat plate. We estimated sand stiffness, k, by fitting a line to the first 17% of data corresponding to a displacement 0.5 cm, before material yielded significantly. We used MATLAB curve fitting and optimization tool boxes to find the best fit of the measured stiffness data. Our choice of fitting function was based on the physical characteristics of the granular media. We first collapsed the stiffness data by dividing it by $d^a w^b$ (*31*). At each inclination angle, θ, k increased quadratically with d and nearly linearly with w (similar to steady state drag on level granular surfaces (*31*)). We then fit the function $c \cos(\pi\, \theta / 2\theta_0)$ to the reduced data. The cos term reflects the rapid decrease in force as θ approaches θ_0.

Robot

The CMU modular snake robot (m = 3150 g, L = 94 cm) used for our robotic experiments (Fig. S5c,d) (*22*, *35*, *36*) was composed of 17 identical modules. Each module was 5 cm in diameter and could output over 3 Nm of torque. Each of these modules serves as a single-DOF joint and the joints are chained together such that they rotate alternatively in pitch and yaw directions with respect to a body-fixed frame. This mechanical configuration enables the snake robot to form three-dimensional shapes. The robot's tail module includes a tether connection with integrated slip-ring.

Supplementary Text

Fig. S1 shows a sidewinder rattlesnake and CMU robot traversing loose sand at inclination of 20 degrees. The lifting regions for both snake and robot are highlighted by red bars.

As shown in Fig. S4c spacing of snake tracks S_t did not change significantly with incline angle (ANOVA, $F_{2,51} = 0.73$, $p = 0.49$). However, wave frequency of the snake decreased with increasing θ (Fig. S4b, ANOVA, $F_{2,51} = 5.93$, $p = 0.005$). The decrease in wave frequency led to a decreased forward speed with increasing incline angle (Fig. S4a, ANOVA, $F_{2,51} = 7.84$, $p = 0.001$). As shown in Fig. S4d, the angle between snake tracks and the direction of motion was also $\alpha = 33 \pm 8$ degrees on granular media and did not significantly change across inclines (ANOVA, $F_{2,51} = 0.09$, $p = 0.77$). Open source Tracker, a video analysis and modeling tool (https://www.cabrillo.edu/~dbrown/tracker/), was used to manually analyze each video and find S_t and α.

Choset's group at CMU has developed a family of limbless robots called modular snake robots (*22*, *35*, *36*). These robots comprise 17 independent modules, each with a single joint arranged orthogonal to the previous one. A schematic of sidewinding gait, sidewinding backbone, and CMU robot schematic are shown in Fig. S5.

Normalized contact length of the robot is plotted versus aspect ratio in Fig. S6a. The plot shows only the minimum required contact lengths for successful climbing. As we increased aspect ratio, the vertical wave amplitude increased. As a result of this increased lifting action, the normalized contact length l/L decreased. With increasing θ we had to decrease the aspect ratio of the elliptical helix for successful climbing (corresponding to an increase in minimum required l/L). The minimum required l/L for successful climbing of the CMU robot is plotted versus θ in Fig. S6b. The wave frequency did not have an impact on l/L within the range of frequencies the robot can handle without significant joint error. As shown in Fig. S6c, speed of the robot at each frequency decreased with increasing θ. Speed also depended on frequency and the higher the frequency, the higher the speed. The reason speed of the robot was decreased with increasing θ at each frequency (Fig. S6c) was the decrease in spacing of tracks at higher inclinations (Fig. S6d). As shown in Movie S1, there was more local slipping at higher inclinations (even in the range we call effective locomotion on Fig. 2f). Thus, the spacing of the tracks was reduced by increasing the inclination.

Table S1 presents locomotor performance of thirteen species of pit vipers on sand at zero and ten degree inclinations. These results show that while several viper (and non-viper) species can sidewind (*9*, *37*), this ability is neither universal nor even common. Further examination and broader taxonomic sampling is the subject of future work.

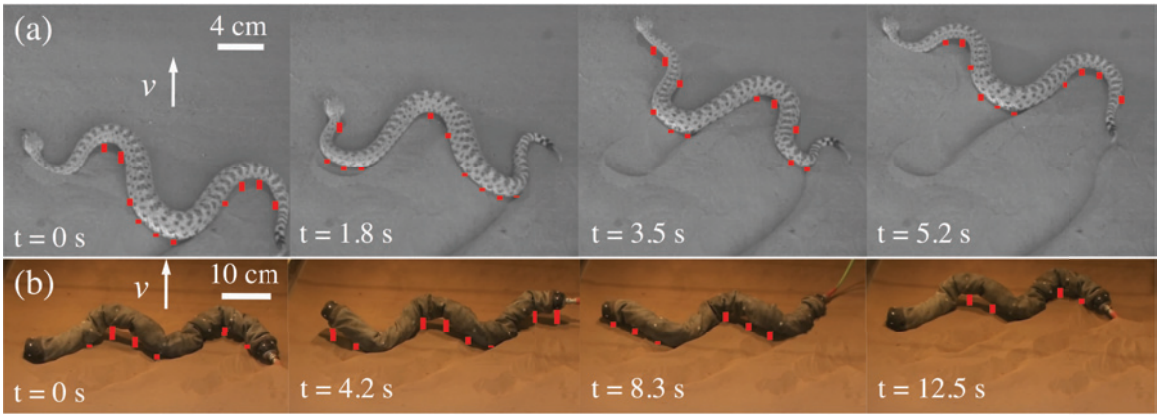

Fig. S1.

(a) A sidewinder rattlesnake and (b) CMU snake robot traversing a 20 degree granular slope. The lifting regions are highlighted by red bars.

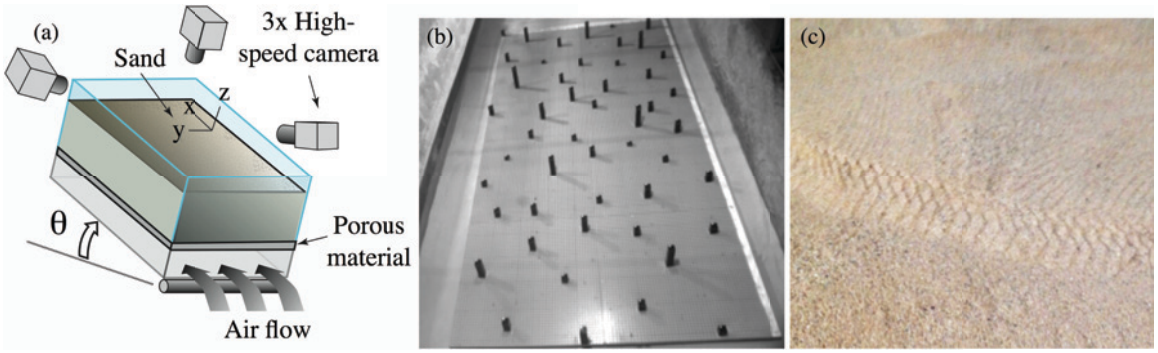

Fig. S2

(a) The experimental apparatus including a diagram of a tiltable fluidized bed trackway and the 3D high-speed imaging system. (b) The calibration object covering the entire bed. (c) Marks of a sidewinder ventral scales during sidewinding, indicating static (peeling/rolling) contact.

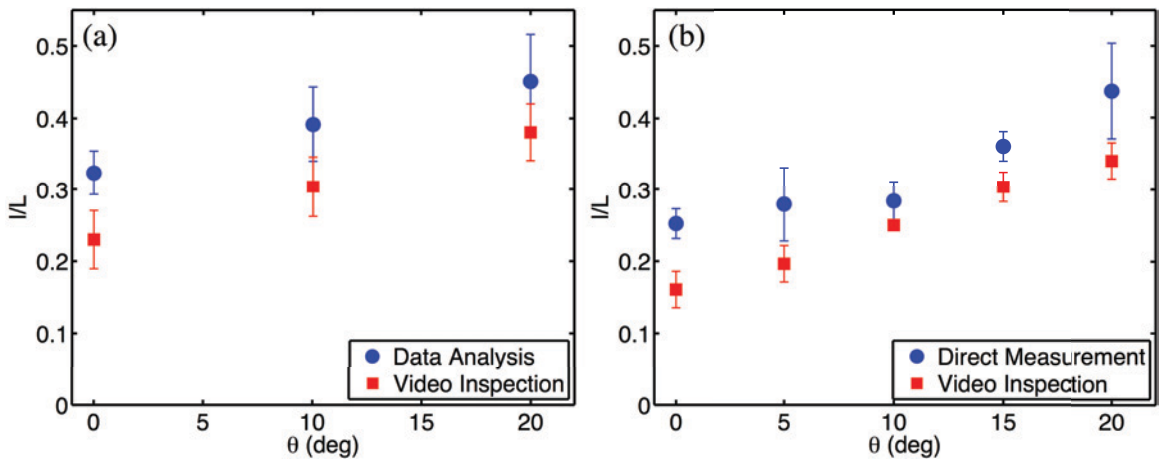

Fig. S3

Comparison of data analyzed using the two different methods described in the supporting methods text for (a) snakes and (b) robot. Data indicate mean +/- SD.

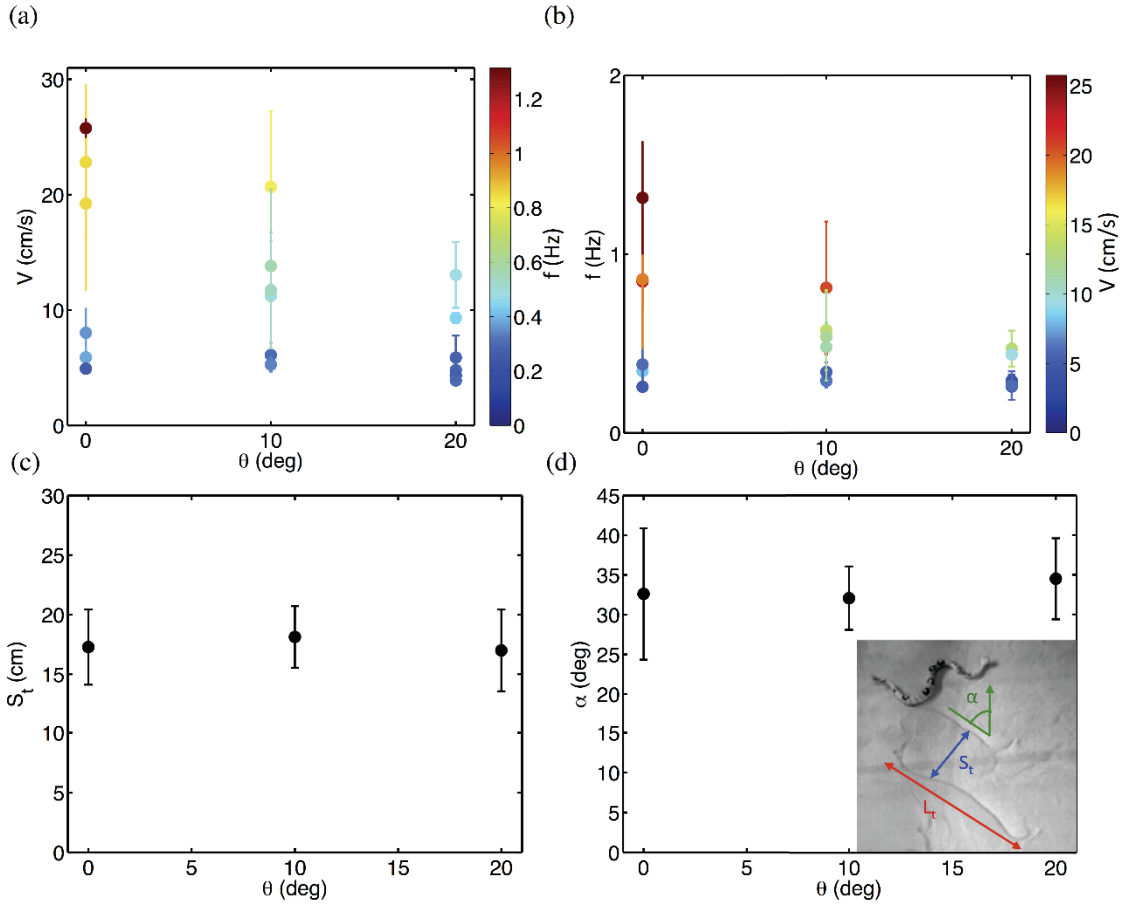

Fig. S4

Snake (a) speed V color coded with wave frequency f, (b) wave frequency color coded with speed, (c) spacing of tracks S_t, and (d) angle between tracks and direction of motion α versus inclination angle θ. Data indicate mean +/- SD.

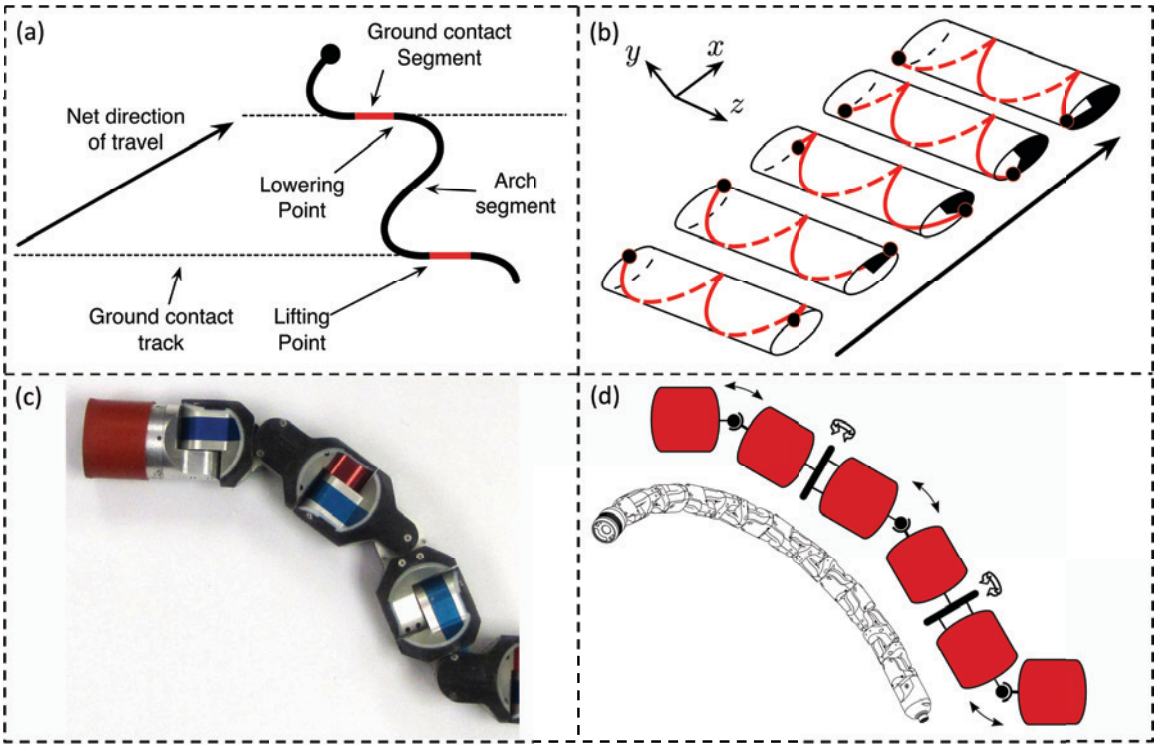

Fig. S5

(a) A schematic of the sidewinding gait showing the direction of travel, direction of traveling wave, and regions of locomotor in contact with ground (*38*). (b) The sidewinding backbone curve is an elliptical helix which acts as a helical tread around a hypothetical core cylinder, driving it forward (*38*). (c)-(d) The CMU robot. Each module has one degree of freedom and is oriented 90 degrees with respect to the previous one to allow motion in three dimensions. Each joint has a full ±90◦ range of motion. The front module of the robot has a camera with LED lighting, and the tail module includes a tether connection with integrated slip-ring.

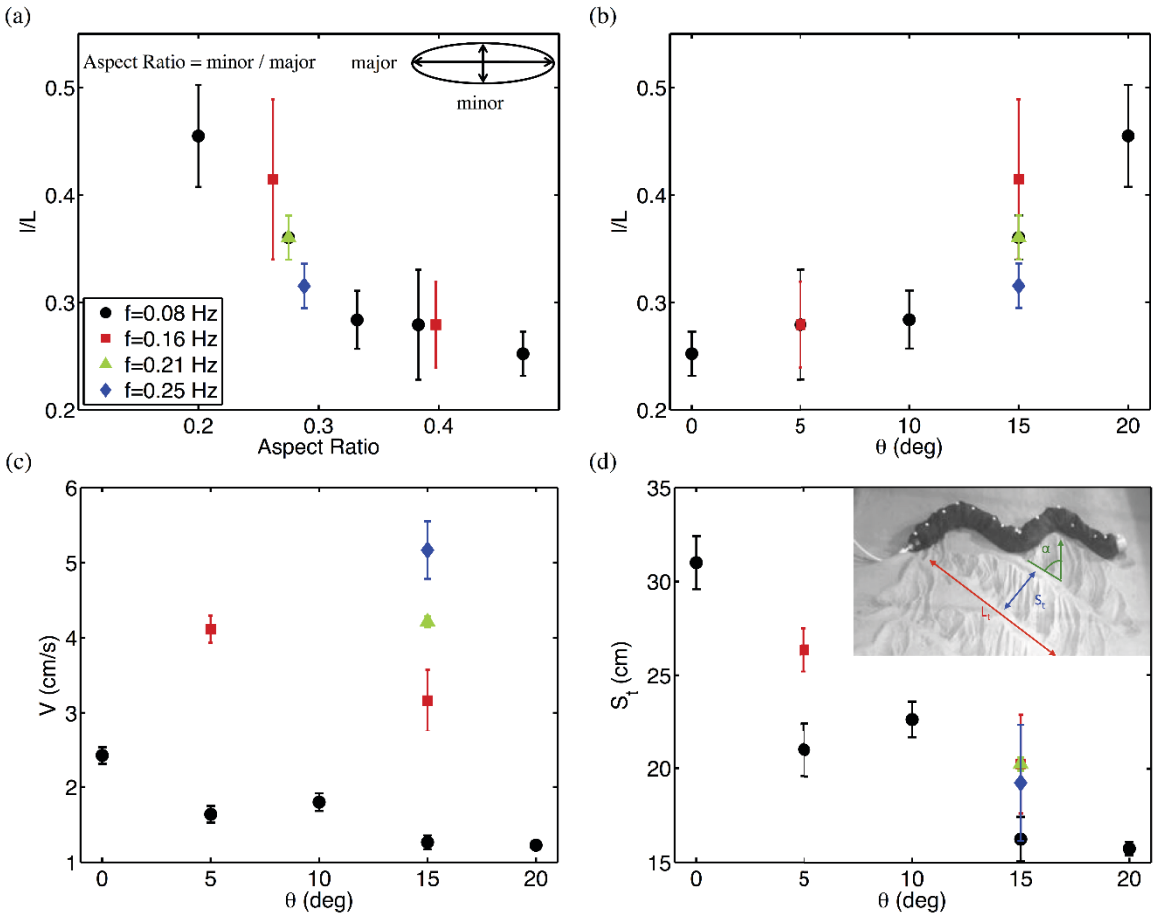

Fig. S6

(a) The normalized contact length l/L of CMU snake robot versus aspect ratio of the elliptical helix at different frequencies. Snake robot's (b) normalized contact length l/L, (c) speed V, and (d) spacing of tracks S_t versus inclination angle θ. The data presented in (a)-(d) are for successful climbing trials (without slipping or pitching down the hill). Data indicate mean +/- SD.

Table S1.

The locomotor behavior of thirteen species of pit vipers on sand at zero and ten degree inclines.

	Level Sand		**10 Degree Incline Sand**	
Species	**Mode of Locomotion**	**Success / Failure**	**Mode of Locomotion**	**Success / Failure**
Agkistrodon contortrix	Lateral Undulation	Success	Lateral Undulation	Failure
Agkistrodon piscivorus	Concertina	Success	Lateral Undulation / Concertina	Failure
Crotalus cerastes	Sidewinding	Success	Sidewinding	Success
Crotalus horridus	Concertina	Success	Concertina	Failure
Crotalus lepidus	Lateral Undulation	Success	Lateral Undulation	Failure
Crotalus mitchellii	Concertina / Rectilinear	Success	Concertina / Rectilinear	Success
Crotalus oreganus	NA	NA	Concertina	Failure
Crotalus polystictus	Lateral Undulation	Success	Lateral Undulation	Failure
Crotalus pricei	Concertina	Success	Lateral Undulation	Failure
Crotalus viridis	Rectilinear	Success	Concertina / Rectilinear	Failure
Crotalus willardi	Lateral Undulation / Concertina	Success	Lateral Undulation	Failure
Mixcoatlus melanurus	Concertina / Rectilinear	Failure	Concertina / Rectilinear	Failure
Sistrurus catenatus	Lateral Undulation	Success	Lateral Undulation	Failure
Sistrurus miliarius	Lateral Undulation	Failure	Lateral Undulation	Failure

Table S2.

Particle size distribution of sand from Yuma County, Arizona (*28*).

Particle diameter (mm)	Mass percentage (%)
< 0.06	2
0.06–0.3	68
0.3–3.0	17
>3.0	13

Movie S1
A sidewinder rattlesnake climbing on loose sand. The videos illustrate sidewinding motion of a snake on inclinations of 0, 10, and 20° at real-time speed followed by 4-times slower speed. The side by side videos show each trial from two different angles.

Movie S2
The CMU robot climbing loose sand at wave frequency of $f = 0.08$ Hz. At inclination of 10 degrees the robot pitched at contact length of $l/L = 0.28$ and slipped at $l/L = 1$. The CMU robot could successfully climb inclination of 10° at $l/L = 0.55$. The last two videos show the robot climbing inclinations of 5 and 20° at similar contact lengths successfully ($l/L = 0.49$ and 0.45, respectively). However, due to the presence of local slipping at the higher inclination angle ($\theta = 20^o$) the step length is shorter and thus the speed is slower.

Movie S3
Movements of Other Crotaline Vipers on Horizontal and Inclined Sand. Sequence 1- A rock rattlesnake (*Crotalus lepidus*) uses lateral undulation on level sand. Sequence 2 - A speckled rattlesnake (*Crotalus mitchellii*) uses concertina with rectilinear locomotion on level sand (2x speed). Sequence 3 - A Mexican pitviper (*Mixcoatlus melanurus*) attempts to move using concertina locomotion on horizontal sand, but fails to make forward progress (3x speed). Sequence 4 - A pigmy rattlesnake (*Sistrurus miliarius*) attempts to move using lateral undulation on horizontal sand, but fails to make forward progress. Sequence 5 - A speckled rattlesnake (*Crotalus mitchellii*) uses concertina with rectilinear locomotion on 10° inclined sand (2x speed). Sequence 6 - A ridge-nosed rattlesnake (*Crotalus willardi*) attempts to move using lateral undulation on 10° inclined sand (uphill is upwards in the video), but fails to make forward progress. Sequence 7 - A Mexican pitviper (*Mixcoatlus melanurus*) attempts to move using concertina locomotion on 10° inclined sand, but fails to make forward progress. Sequence 8 - A pigmy rattlesnake (*Sistrurus miliarius*) attempts to move using lateral undulation on 10° inclined sand (uphill is upwards in the video), but fails to make forward progress.

Movie S4
Fluidizing sand using an air-fluidized bed. We constructed a setup to prepare a uniform and consistent state for the granular media before each trial. Our fluidized bed has a porous floor allowing the air to uniformly flow through the entire sand and letting it re-settle into an equilibrium condition. As shown in this video, regardless of the initial state of the sand we were able to achieve a loosely packed granular media with a smooth surface after the fluidization process.

Movie S5
A sidewinder rattlesnake climbing loose sand at an inclination of 27°. The video is sped up 4 times and illustrates the extended contacts the snake makes during sidewinding motion on the highest possible angle (angle of maximum stability) on loose sand.

References and Notes

1. M. Costello, J. Sahu, Using computational fluid dynamic/rigid body dynamic results to generate aerodynamic models for projectile flight simulation. *Proc. Inst. Mech. Eng. Part G J. Aerosp. Eng.* **222**, 1067–1079 (2008). doi:10.1243/09544100JAERO304

2. J. E. Clark *et al*., *Proceedings of IEEE International Conference on Robotics and Automation* (2001), vol. 4, pp. 3643–3649.

3. B. Bhushan, Biomimetics: Lessons from nature-an overview. *Philos. Trans. R. Soc. Math. Phys. Eng. Sci.* **367**, 1445–1486 (2009). doi:10.1098/rsta.2009.0011

4. R. Playter, M. Buehler, M. Raibert, *Unmanned Ground Vehicle Technology VIII*, D. W. G. Grant R. Gerhart, Charles M. Shoemaker, Eds., vol. 6230 of *Proceedings of SPIE* (2006), pp. 62302O1–62302O6.

5. M. Tesch, K. Lipkin, I. Brown, R. Hatton, A. Peck, J. Rembisz, H. Choset, Parameterized and scripted gaits for modular snake robots. *Adv. Robot.* **23**, 1131–1158 (2009). doi:10.1163/156855309X452566

6. K. Y. Ma, P. Chirarattananon, S. B. Fuller, R. J. Wood, Controlled flight of a biologically inspired, insect-scale robot. *Science* **340**, 603–607 (2013). Medline doi:10.1126/science.1231806

7. R. D. Maladen, Y. Ding, C. Li, D. I. Goldman, Undulatory swimming in sand: Subsurface locomotion of the sandfish lizard. *Science* **325**, 314–318 (2009). Medline doi:10.1126/science.1172490

8. P. Holmes, R. J. Full, D. Koditschek, J. Guckenheimer, The dynamics of legged locomotion: Models, analyses, and challenges. *SIAM Rev.* **48**, 207–304 (2006). doi:10.1137/S0036144504445133

9. B. C. Jayne, Kinematics of terrestrial snake locomotion. *Copeia* **1986**, 915–927 (1986). doi:10.2307/1445288

10. D. L. Hu, J. Nirody, T. Scott, M. J. Shelley, The mechanics of slithering locomotion. *Proc. Natl. Acad. Sci. U.S.A.* **106**, 10081–10085 (2009). Medline doi:10.1073/pnas.0812533106

11. B. Jayne, Swimming in constricting (*Elaphe* g. *guttata*) and nonconstricting (*Nerodia fasciata pictiventris*) colubrid snakes. *Copeia* **1985**, 195–208 (1985). doi:10.2307/1444809

12. K. S. Norris, J. L. Kavanau, The burrowing of the Western shovel-nosed snake, *Chionactis occipitalis* Hallowell, and the undersand environment. *Copeia* **1966**, 650–664 (1966). doi:10.2307/1441397

13. H. Marvi, D. L. Hu, Friction enhancement in concertina locomotion of snakes. *J. R. Soc. Interface* **9**, 3067–3080 (2012). Medline doi:10.1098/rsif.2012.0132

14. G. Byrnes, B. C. Jayne, Substrate diameter and compliance affect the gripping strategies and locomotor mode of climbing boa constrictors. *J. Exp. Biol.* **213**, 4249–4256 (2010). Medline doi:10.1242/jeb.047225

15. J. J. Socha, Gliding flight in the paradise tree snake. *Nature* **418**, 603–604 (2002). Medline doi:10.1038/418603a

16. W. Mosauer, A note on the sidewinding locomotion of snakes. *Am. Nat.* **64**, 179–183 (1930). doi:10.1086/280308

17. S. M. Secor, B. C. Jayne, A. F. Bennett, Locomotor performance and energetic cost of sidewinding of the snake *Crotalus cerastes*. *J. Exp. Biol.* **163**, 1–14 (1992). doi:10.1016/0022-0981(92)90143-X

18. H. Marvi, J. Bridges, D. L. Hu, Snakes mimic earthworms: Propulsion using rectilinear travelling waves. *J. R. Soc. Interface* **10**, 20130188 (2013). Medline doi:10.1098/rsif.2013.0188

19. J. Gray, The mechanism of locomotion in snakes. *J. Exp. Biol.* **23**, 101–120 (1946). Medline

20. B. C. Jayne, Muscular mechanisms of snake locomotion: An electromyographic study of the sidewinding and concertina modes of *Crotalus cerastes*, *Nerodia fasciata* and *Elaphe obsoleta*. *J. Exp. Biol.* **140**, 1–33 (1988). Medline

21. J. Burdick, J. Radford, G. Chirikjian, A 'sidewinding' locomotion gait for hyper-redundant robots. *Adv. Robot.* **9**, 195–216 (1994). doi:10.1163/156855395X00166

22. R. L. Hatton, H. Choset, *IEEE International Conference on Robotics and Automation* (2010), pp. 691–696.

23. Materials and methods are available as supplementary materials on *Science* Online.

24. C. Li, P. B. Umbanhowar, H. Komsuoglu, D. E. Koditschek, D. I. Goldman, From the cover: Sensitive dependence of the motion of a legged robot on granular media. *Proc. Natl. Acad. Sci. U.S.A.* **106**, 3029–3034 (2009). Medline doi:10.1073/pnas.0809095106

25. S. Sefati, I. D. Neveln, E. Roth, T. R. Mitchell, J. B. Snyder, M. A. Maciver, E. S. Fortune, N. J. Cowan, Mutually opposing forces during locomotion can eliminate the tradeoff between maneuverability and stability. *Proc. Natl. Acad. Sci. U.S.A.* **110**, 18798–18803 (2013). Medline doi:10.1073/pnas.1309300110

26. N. Mazouchova, P. B. Umbanhowar, D. I. Goldman, Flipper-driven terrestrial locomotion of a sea turtle-inspired robot. *Bioinspir. Biomim.* **8**, 026007 (2013). Medline doi:10.1088/1748-3182/8/2/026007

27. R. Albert, M. Pfeifer, A.-L. Barabási, P. Schiffer, Slow drag in a granular medium. *Phys. Rev. Lett.* **82**, 205–208 (1999). doi:10.1103/PhysRevLett.82.205

28. C. Li, T. Zhang, D. I. Goldman, A terradynamics of legged locomotion on granular media. *Science* **339**, 1408–1412 (2013). Medline doi:10.1126/science.1229163

29. H. Katsuragi, D. J. Durian, Unified force law for granular impact cratering. *Nat. Phys.* **3**, 420–423 (2007). doi:10.1038/nphys583

30. D. L. Henann, K. Kamrin, A predictive, size-dependent continuum model for dense granular flows. *Proc. Natl. Acad. Sci. U.S.A.* **110**, 6730–6735 (2013). Medline doi:10.1073/pnas.1219153110

31. D. J. Costantino, J. Bartell, K. Scheidler, P. Schiffer, Low-velocity granular drag in reduced gravity. *Phys. Rev. E Stat. Nonlin. Soft Matter Phys.* **83**, 011305 (2011). Medline doi:10.1103/PhysRevE.83.011305

32. A. G. Winter 5th, R. L. H. Deits, A. E. Hosoi, Localized fluidization burrowing mechanics of Ensis directus. *J. Exp. Biol.* **215**, 2072–2080 (2012). Medline doi:10.1242/jeb.058172

33. N. Mazouchova, N. Gravish, A. Savu, D. I. Goldman, Utilization of granular solidification during terrestrial locomotion of hatchling sea turtles. *Biol. Lett.* **6**, 398–401 (2010). Medline doi:10.1098/rsbl.2009.1041

34. T. L. Hedrick, Software techniques for two- and three-dimensional kinematic measurements of biological and biomimetic systems. *Bioinspir. Biomim.* **3**, 034001 (2008). Medline doi:10.1088/1748-3182/3/3/034001

35. A. Wolf *et al*., *IEEE/RSJ International Conference on Intelligent Robots and Systems* (2003), vol. 3, pp. 2889–2895.

36. C. Wright *et al*., *IEEE/RSJ International Conference on Intelligent Robots and Systems* (2007), pp. 2609–2614.

37. C. Gans, H. Mendelssohn, in *Toxins of Animal and Plant Origin*, A. de Vries, E. Kochva, Eds. (Gordon and Breach Science Publishers, London, 1972), pp. 17–38.

38. C. Gong, R. L. Hatton, H. Choset, *IEEE International Conference on Robotics and Automation* (2012), pp. 4222–4227.